

Modelling and experiments of self-reflectivity under femtosecond ablation conditions

H. Zhang,^{1,*} S. A. Wolbers,¹ D. M. Krol,^{1,2} J. I. Dijkhuis,¹ and D. van Oosten^{1,†}

¹*Debye Institute for Nanomaterials Science, Utrecht University,*

P. O. Box 80000, 3508 TA Utrecht, The Netherlands

²*University of California Davis, Davis, CA 95616*

We present a numerical model which describes the propagation of a single femtosecond laser pulse in a medium of which the optical properties dynamically change within the duration of the pulse. We use a Finite Difference Time Domain (FDTD) method to solve the Maxwell's equations coupled to equations describing the changes in the material properties. We use the model to simulate the self-reflectivity of strongly focused femtosecond laser pulses on silicon and gold under laser ablation condition. We compare the simulations to experimental results and find excellent agreement.

I. INTRODUCTION

Recent advances in ultrafast laser material processing enable nano-sized structures to be directly fabricated in various materials¹⁻⁴. The basic processes during femtosecond laser ablation are absorption by electrons, energy transfer to the lattice and subsequent material removal. These processes are all temporally well separated⁵. The first step, the absorption of light, is a complex and interesting problem. As the laser pulses are focused into a spot size comparable to the wavelength of the laser light, the interaction between the light and the material takes place in a very confined volume. Furthermore, due to the high peak intensities involved, nonlinear optical effects play a dominant role. Typically, when a laser pulse propagates through a semiconductor or an insulator, multi-photon absorption takes place during the leading part of the pulse. This leads to the generation of a high concentration of charge carriers. When a laser pulse impinges on a metal, the existing free electrons in the metal will be strongly heated by the leading part of the pulse. In both cases the leading part of the pulse alters the optical properties of the material, which implies that the trailing part of the laser pulse interacts with a material whose optical properties are significantly different from those of the unexcited material. A detailed numerical modeling of this process provides insights into the complex mechanism of energy deposition under these conditions and is therefore crucial to describe laser nano-processing.

In earlier one-dimensional models of the absorption of femtosecond laser pulses in silicon, the dynamically changing optical properties were taken into account using a nonlinear Lambert-Beer law, with absorption coefficients that change dynamically due to the generation of free carriers. The results of these models are in good agreement with reflectivity measurements performed with weakly focused laser beams⁶⁻⁸. However, these one-dimensional models are expected not to be adequate to describe the laser-matter interaction in sub-wavelength volumes and with the large focusing angles obtained with high numerical aperture objectives. In other studies, the propagation of femtosecond laser pulses in nonlinear media is simulated by solving the non-

linear Schrödinger equation (NLSE)^{9,10}. However, the self-scattering by the sub-wavelength plasma formed during nano-ablation¹¹ implies the breakdown of the slowly-varying-amplitude-approximation on which the NLSE is based. Additionally, the high numerical aperture objective used to focus the beam implies the breakdown of the paraxial approximation, another approximation used in the derivation of the NLSE. Due to these limitations of the NLSE, there is an increasing interest in the development of numerical models that resolve the full set of Maxwell's equations coupled to the equations describing the changes in the materials induced by the pulse under tight focusing conditions¹²⁻¹⁵. However existing studies do not address laser-matter interaction in metals, do not find quantitative agreement with experiments or lack a comparison to experiments.

In this paper, we present a numerical model of the laser energy deposition in femtosecond laser nano-processing of both semiconductors and metals. The model simulates the propagation of light using a two-dimensional Finite Difference Time Domain (FDTD) method, coupled to a set of differential equations that describe the changes in the material properties that are driven by the laser light. The model is compared with self-reflectivity measurements of a strongly focused femtosecond laser beam in single-shot ablation experiments on silicon and gold. We show that the model excellently describes the self-reflectivity measurements on the four types of specimens we investigated, namely two silicon-on-insulator samples with different device layer thickness, bulk silicon and gold. We further show that in the case of strong focusing, a one-dimensional model does not reproduce the experimental results and that a two-dimensional model is thus required. As our model excellently agrees with the experimental results, without the use of fitting parameters, it can be used to study and optimize the energy deposition in femtosecond laser nano-processing of materials.

The paper is organized as follows. In Section II we discuss the theoretical model we use to describe the propagation of an intense laser pulse in a medium of which the optical properties are changing during the pulse. In Section III, we describe in detail the numerical implementation of that model. In Section IV, we compare the

results of the model to experimental results. A summary and conclusion are presented in Section V.

II. THEORY

The propagation of electromagnetic waves is in general governed by Maxwell's equations

$$\nabla \times \mathbf{H} = \frac{\partial \mathbf{D}}{\partial t} + \mathbf{j}, \quad \nabla \times \mathbf{E} = -\frac{\partial \mathbf{B}}{\partial t},$$

in combination with relations defining the auxiliary fields

$$\mathbf{D} = \epsilon_0 \mathbf{E} + \mathbf{P}, \quad \mathbf{H} = \frac{1}{\mu_0} \epsilon_0 \mathbf{B} - \mathbf{M}.$$

The above relations are specific to the medium and can be modelled using microscopic theories. In a linear and homogeneous medium, we can write $\mathbf{P} = \epsilon_0 \chi \mathbf{E}$ and $\mathbf{M} = \chi_m \mathbf{B} / \mu_0$, where χ is the electric susceptibility and χ_m is the magnetic susceptibility. For electromagnetic waves at optical frequencies, the magnetic susceptibility is almost always negligibly small. We will therefore neglect it in the remainder of this paper and only consider the electric susceptibility. In the simple linear and homogeneous case, the above set of equations can be easily cast into a wave equation which can then be solved analytically. However, in relevant cases, the susceptibility is not homogeneous. In that situation, one in general needs numerical methods to solve Maxwell's equations. Furthermore, when sufficiently strong fields are applied, nonlinear effects can come into play. For example, absorption of light by the medium can result in the generation of free charge-carriers. These free carriers will contribute to the susceptibility. As this will make the susceptibility depend on the intensity of light inside the medium, free-carrier generation also leads to inhomogeneity even in case of an initially homogeneous medium. Local heating of the material has a similar effect, as it locally changes the refractive index and thus makes the medium inhomogeneous.

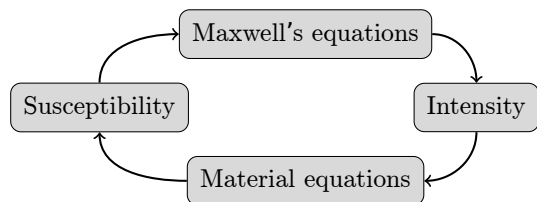


FIG. 1. Diagrammatic view of the model

In many cases, the change in the local susceptibility are small and slow enough to be negligible when considering the propagation of light. However, when using focused pico- or femtosecond pulses, the changes in local susceptibility occur during the pulse itself. As illustrated in Fig. 1, this requires one to solve the equations governing the dynamics of the properties of the material, which

is driven by the intensity of light. This intensity is obtained by solving the Maxwell's equations, which use the material properties as an input.

If we assume that the susceptibility changes slowly with respect to the oscillation period of the light, we can neglect time derivatives of the susceptibility and thus write the time derivative of the displacement field as $\partial \mathbf{D} / \partial t = (1 + \chi) \partial \mathbf{E} / \partial t$. This reduces the Maxwell's equations to

$$\frac{\partial \mathbf{H}(\mathbf{r}, t)}{\partial t} = \frac{1}{\mu_0} \nabla \times \mathbf{E}(\mathbf{r}, t), \quad (1)$$

$$\frac{\partial \mathbf{E}(\mathbf{r}, t)}{\partial t} = \frac{1}{\epsilon_0 \epsilon_r(\mathbf{r}, t)} \nabla \times \mathbf{H}(\mathbf{r}, t), \quad (2)$$

where we have introduced the dielectric function $\epsilon_r(\mathbf{r}, t) = 1 + \chi(\mathbf{r}, t)$.

To determine the susceptibility, we need to determine certain position- and time-dependent properties of the material. For instance, we require the carrier density $N(\mathbf{r}, t)$, which we can obtain by integrating the diffusion equation

$$\frac{\partial N(\mathbf{r}, t)}{\partial t} + \nabla \cdot [-D_0(\mathbf{r}, t) \nabla N(\mathbf{r}, t)] = S_N(\mathbf{E}(\mathbf{r}, t)), \quad (3)$$

where the source term S_N depends on the intensity of light (and thus on the electric-field amplitude) as absorption of light leads to the formation of free carriers.

The carrier density distribution obtained from the diffusion equation is subsequently used to calculate position- and time-dependent susceptibility (and thus the dielectric function)

$$\epsilon_r(\mathbf{r}, t) = 1 + \chi(\mathbf{r}, N(\mathbf{r}, t), \dots), \quad (4)$$

where we have now explicitly written the susceptibility as a function of the carrier density. The dots indicate that the susceptibility is also a function of other properties of the medium, such as electron temperature, lattice temperature, etc.. If these are expected to vary on the timescale of the pulse, additional equations need to be included to describe their dynamics.

In the next section, we will follow the outline given above to derive a model to describe the self-reflectivity of a semiconductor structure subjected to intense femtosecond laser illumination. We will explicitly discuss the physical processes that should be taken into account and give details of the numerical implementation of the model.

III. THE MODEL

As described in the previous section, we need to solve a set of equations to describe how the dielectric function evolves during the laser pulse. Which equations we need to solve depends on the material used. Here we describe the relevant sets of equations required to model the self-reflectivity of a semiconductor as well as a metal under

ablation conditions and show that the model is in excellent agreement with experimental results for both types of materials.

A. Laser-matter interaction for silicon

The first process during the absorption of a femtosecond laser pulse by a semiconductor is the excitation of electrons from the valence band to the conduction band. Depending on the band gap of the material and the incident photon energy, the excitation can be either one-photon absorption or multi-photon absorption or both. Subsequently, electrons already excited to the conduction band can gain energy in the laser field via free-carrier absorption. If the excess energy of a conduction electron is sufficiently high, it may excite another electron in the valence band to the conduction band, by a process known as impact ionization. When this process occurs multiple times, it is referred to as avalanche or cascade ionization. For silicon at 800 nm excitation wavelength, free carriers are created by one-photon absorption (OPA), two-photon absorption (TPA)^{7,16}, and impact ionization¹⁷. Generally, impact ionization is a very complicated process that involves the energy distribution of the electrons¹⁸. Here we use a simplified and convenient expression for the impact ionization term, deduced by Stuart *et al.*¹⁹. We rewrite Eq. (3) as

$$\frac{\partial N(\mathbf{r}, t)}{\partial t} + \nabla \cdot [-D\nabla N(\mathbf{r}, t)] = \frac{\alpha_0 I(\mathbf{r}, t)}{\hbar\omega} + \frac{\beta I^2(\mathbf{r}, t)}{2\hbar\omega} + \theta I(\mathbf{r}, t)N(\mathbf{r}, t), \quad (5)$$

where D is the carrier diffusivity, α_0 is the OPA coefficient, β is the TPA coefficient, and θ is the impact ionization coefficient. The intensity $I(\mathbf{r}, t)$ that appears in the source term on the right-hand side of the above equation is the laser intensity inside the medium, which can be obtained from the amplitude of the time-varying electric field in the material using

$$I(\mathbf{r}, t) = \frac{1}{2}\epsilon_0 c \text{Re}\{n(\mathbf{r}, t)\} |E_0(\mathbf{r}, t)|^2, \quad (6)$$

where $\text{Re}\{n\}$ denotes the real part of the refractive index n . We deduce the impact ionization coefficient θ from the experimental results obtained by Pronko *et al.* who measured the impact ionization rate (s^{-1}) for the dielectric breakdown in silicon with 786 nm fs laser pulses.¹⁷ In Fig. 2, we plot their results as a function of intensity. Fitting the data yields an impact ionization coefficient $\theta = 21.2 \text{ cm}^2/\text{J}$. Due to the creation of a high density of carriers, the optical response of silicon under ablation conditions is dominated by the free-carrier response, which can be calculated using the Drude model^{7,16}. In our model, we also take into account the changes in the dielectric constant due to the optical Kerr effect and TPA. Thus the dielectric function of strongly excited sil-

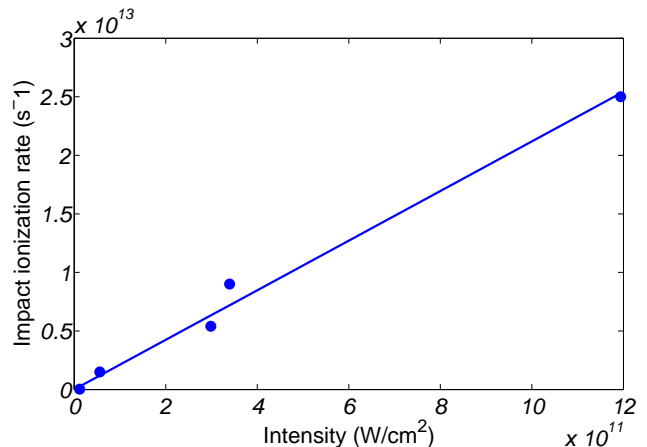


FIG. 2. Impact ionization rate in silicon. An impact ionization rate $\theta = 21.2 \text{ cm}^2/\text{J}$ is obtained by a linear fit of the data presented in Ref.¹⁷.

icon (ϵ_{ex}) can be written as

$$\epsilon_{\text{ex}}(\mathbf{r}, t) = \epsilon_{\text{Si}} + \epsilon_{\text{Drude}} + \epsilon_{\text{NL}}, \quad (7)$$

$$\epsilon_{\text{Drude}}(\mathbf{r}, t) = -\frac{(\omega_p/\omega)^2}{1 + i/\omega\tau_d}, \quad (8)$$

$$\epsilon_{\text{NL}}(\mathbf{r}, t) = \frac{3}{4}\chi_3 |E_0(\mathbf{r}, t)|^2, \quad (9)$$

$$\omega_p(\mathbf{r}, t) = \sqrt{\frac{N(\mathbf{r}, t)e^2}{m^*m_e\epsilon_0}}, \quad (10)$$

where ϵ_{Si} is the dielectric constant of unexcited silicon at 800 nm ($13.6 + 0.048i$)¹⁶ and τ_d is the carrier collision time, which is believed to be around 1 fs^{6,7} at the excitation level relevant for this work. Finally m^*m_e is the optical effective mass of highly excited silicon, which we will discuss later in this section. The third-order susceptibility χ_3 can be calculated from the value of the Kerr coefficient n_2 and the value of TPA coefficient β in silicon. The refractive index n and the effective absorption coefficient α_{ex} of the excited material are

$$n_{\text{ex}} = \sqrt{\epsilon_{\text{ex}}}, \quad (11)$$

$$\alpha_{\text{ex}} = \frac{4\pi \text{Im}\{n_{\text{ex}}\}}{\lambda_0}. \quad (12)$$

Although the carrier temperature does not explicitly appear in the above equations for the dielectric function, we nevertheless have to calculate it. This is because the carrier diffusivity D and the optical effective mass m^*m_e depend on the carrier temperature. To model the change of the carrier temperature T_c during the pulse, we use a heat equation^{7,16}

$$\frac{\partial [U_c(\mathbf{r}, t)]}{\partial t} + \nabla \cdot [-\kappa_c \nabla T_c(\mathbf{r}, t)] = \alpha_{\text{ex}} I(\mathbf{r}, t). \quad (13)$$

The total energy density U_c of the excited carriers is given by

$$U_c = C_c T_c + N E_g, \quad (14)$$

with C_c the carrier heat capacity, E_g the band gap energy and κ_c the thermal conductivity of the carriers. As the carrier temperature reached at the excitation level relevant to this work exceeds 10^4 K, the induced plasma is nondegenerate even at high densities⁷. Thus, the carrier heat capacity and the carrier heat conductivity can be approximated using classical thermodynamics²⁰,

$$C_c = 3k_B N(\mathbf{r}, t), \quad (15)$$

$$\kappa_c = \frac{1}{3} C_c \langle v_c \rangle^2 \tau_d, \quad (16)$$

where k_B is the Boltzmann constant, $\langle v_c \rangle = \sqrt{3k_B T_c / m^*}$ the thermal velocity of carriers, m^* the carrier effective mass and τ_d the carrier-carrier collision time. The carrier diffusivity is then found using the Einstein relation²⁰

$$D = \frac{k_B T_c \tau_d}{m^*}. \quad (17)$$

In Ref.⁷ the authors determine a static optical effective mass of the femtosecond laser-induced plasma in silicon using time-resolved pump-probe experiments. However, as the optical effective mass is both temperature and density dependent, it will actually change during the pulse. For the carrier temperatures relevant for this work, the Fermi-Dirac reduces to a Boltzmann distribution, resulting in an effective mass that is independent of the carrier density²¹. The temperature dependence remains and is easy to understand; when the electrons are heated up far beyond the conduction band edge, the curvature of the band decreases, giving rise to a larger effective mass. In this case, the optical effective mass increases approximately linearly with carrier temperature²¹. As experimental measurements of the optical effective mass are based on the Drude model, they only depend on the ratio N/m^* (see Eq. (10)). So to measure m^* one needs to know the carrier density N , which in our case is a-priori unknown. Therefore, we use the relation suggested by Riffe's theoretical calculation which takes the detailed band structure of silicon into account. His calculation shows that the optical effective mass can in our regime be approximated by

$$m^* = m_0^* + m_k T_c, \quad (18)$$

where the optical effective mass of unperturbed silicon m_0^* is well-known to be $0.15 m_e$ ^{7,21}. We extract the slope $m_k = 3.1 \times 10^{-5} \text{ K}^{-1}$ from Riffe's calculations²¹.

B. Laser-matter interaction for gold

In the case of femtosecond laser ablation of gold, the optical absorption process is somewhat different. As there is already a high density of free electrons present in the unexcited material, the number of free electrons is not significantly influenced by the laser pulse. The dominant absorption mechanism is therefore the heating of

those electrons. In analogy with Eq. (13) we use

$$C_e \frac{\partial [T_e(\mathbf{r}, t)]}{\partial t} + \nabla \cdot [-\kappa_e \nabla T_e(\mathbf{r}, t)] = \alpha_{\text{ex}} I(\mathbf{r}, t), \quad (19)$$

where the subscript e denotes that the only charge carriers are electrons. At the high electron temperatures reached during ablation, we can approximate the electronic heat capacity as

$$C_e = \frac{3}{2} k_B N, \quad (20)$$

where the electron density N is now kept constant during the simulation. The change of electron temperature gives rise to a change in the Drude damping time which is given by

$$\frac{1}{\tau_d} = \frac{1}{\tau_{e-e}} + \frac{1}{\tau_{e-l}}, \quad (21)$$

where $\tau_{e-e}^{-1} = AT_e^2$ and $\tau_{e-l}^{-1} = BT_l^{22}$ are the scattering rates for electron-electron and electron-phonon interactions, respectively. In the future, the model could be improved by taking the electron heat capacity from detailed band structure calculations²³. The dielectric function can be written as,

$$\epsilon_{\text{ex}}(\mathbf{r}, t) = \epsilon_{\infty} + \epsilon_{\text{Drude}}(\mathbf{r}, t), \quad (22)$$

$$\epsilon_{\text{Drude}}(\mathbf{r}, t) = -\frac{(\omega_p/\omega)^2}{1 + i/\omega\tau_d(\mathbf{r}, t)}, \quad (23)$$

where ϵ_{∞} is an offset to the dielectric function that takes into account the effect of resonances at shorter wavelengths. Note in the case of gold $\omega_p = \sqrt{Ne^2/m^*m_e\epsilon_0}$ is a constant but $\tau_d(\mathbf{r}, t)$ is locally and dynamically changing during the pulse, in contrast to the case of silicon.

C. FDTD model

To solve Eqs. (1) and (2), we use a finite difference time domain (FDTD) method. As dictated by the Courant condition of the FDTD method (see for instance²⁴), the E and H fields are updated hundreds of times per optical cycle. Once every optical half-cycle, we extract the electric-field amplitude $E_o(\mathbf{r}, t)$ from that optical half-cycle. Details of how we extract the amplitude can be found in Appendix A. From the electric-field amplitude, we determine the intensity $I(\mathbf{r}, t)$ using Eq. (6). We use this intensity to march Eq. (5) and 13 (in the case of silicon) or Eq. (19) (in the case of gold) forward in time by a single step using an implicit Euler method. As implicit Euler methods are unconditionally stable, we can choose the time step in the Euler method as half an optical cycle. The other quantities such as diffusivity, heat capacity, heat conductivity, etc. are subsequently calculated. After this, we use the carrier density $N(\mathbf{r}, t)$ (in the case of silicon) or the carrier temperature $T_e(\mathbf{r}, t)$ (in the case of gold) to obtain a new dielectric function

$\epsilon_{\text{ex}}(\mathbf{r}, t)$. This updated dielectric function is used in the next optical half-cycle of the FDTD simulation.

The self-reflectivity of a strongly focused laser pulse is in principle a three-dimensional problem. However, three-dimensional finite difference time domain (FDTD) simulation are notoriously time and memory consuming. We therefore instead run two-dimensional simulations for the TE and TM case and use those to approximate the three-dimensional reflectivity. This requires an extra step that we discuss at the end of this subsection. A schematic

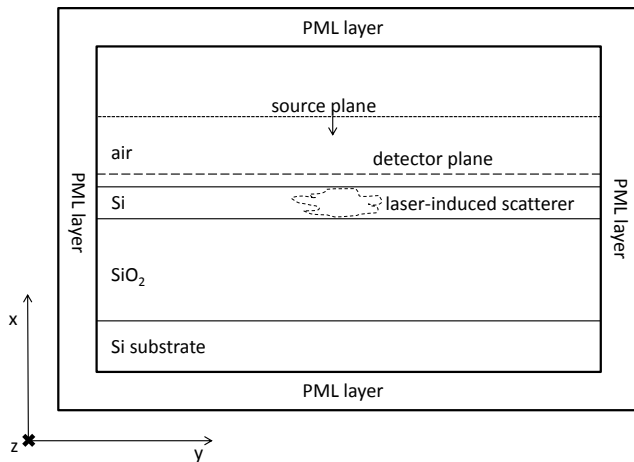


FIG. 3. Layout of the 2D-FDTD simulation box. The FDTD grid is excited by a soft source which is located 200 nm above the silicon-air interface. Scattered \mathbf{E} and \mathbf{H} near-field values are recorded at the detector plane to extract the reflectivity.

representation of our 2D-FDTD simulation box is shown in Fig. 3. The grid sizes for the simulations are chosen to be around 15 nm such that the errors in the absolute reflectivity are smaller than 0.01 (See Appendix B) and the device layer thicknesses can be written as integers times the grid size. The width of the simulation box is $2 \mu\text{m}$ which is two times the size of the focused laser spot ($1 \mu\text{m}$ @ $1/e^2$ of intensity). The incident pulse duration used in the simulation is 126 fs, which is the value measured experimentally using a single-shot autocorrelator. The source plane is located at 200 nm above the sample surface, while the near-field detector plane is located one cell above the sample surface. There are 30 grid points in each of the four perfectly matched layers (PML) to ensure negligible reflections at the boundaries. We tested the accuracy of our method by comparing to several benchmarks, as discussed in Appendix C. Due to the high carrier density in both gold and excited silicon, we need to implement dispersion and loss in our FDTD method. Details of this implementation are given in Appendix D.

To determine the field that will be scattered/reflected back by the sample, we run the simulation with and without the sample and take the difference in the electric field at the detector plane as the scattered near-field. The submicron-sized laser-induced plasma induces com-

ponents with a spatial frequency, which is too high to propagate into the far-field. We therefore filter the high spatial frequency components from the scattered near-fields, as described in Appendix E in order to obtain the scattered far-field. From the resulting fields, we calculate the reflected pulse fluence $\mathcal{F}_{\text{refl}}^{\text{TE, TM}}(y)$ and the incident pulse fluence $\mathcal{F}_{\text{inc}}^{\text{TE, TM}}(y)$. Here, the superscripts TE and TM denote the results for the TE and the TM case. To obtain the total reflected/incident pulse energy, we add the TE and TM contributions. To approximate the three-dimensional results, we treat the y -coordinate in our simulation as the radial coordinate in a polar coordinate system and integrate the reflected/incident fluence over the area of the incident focal spot

$$U_{\text{refl, inc}} = \int_0^{r_{\text{max}}} 2\pi r dr (\mathcal{F}_{\text{refl, inc}}^{\text{TE}}(r) + \mathcal{F}_{\text{refl, inc}}^{\text{TM}}(r)), \quad (24)$$

where r_{max} is chosen to be twice the waist of the focused laser spot. Finally, we obtain the reflectivity

$$R = \frac{U_{\text{refl}}}{U_{\text{inc}}}. \quad (25)$$

This equation yields the value for R to we will compare with experimental measurements in the next section.

IV. RESULTS AND COMPARISON WITH EXPERIMENTS

In the case of silicon we have carried out simulations on thin-film, silicon-on-insulator (SOI) samples as well as bulk silicon. Experimental results for these samples can be found in Ref.¹¹. For the simulations a number of input parameters need to be specified. The values we used are listed in Table I. In addition to these parameters, values for the Si and SiO₂ layer thicknesses are required for the SOI samples. Table II lists the parameters used in our simulations. As can be seen, we inserted values for the layer thicknesses slightly deviating from their measured values. These adjusted values were chosen in order to yield the correct self-reflectivity at vanishing fluence. It should be noted that the reflectivity in this regime depends only on the thicknesses of the layers and the refractive indices of the unperturbed media.

Fig. 4 shows the self-reflectivity calculated using the model and the experimental data of the bulk silicon and the SOI samples. As is shown for the SOI₁ sample, the experimental data lie between the calculated self-reflectivity for the TM and the TE mode and agree well with the calculation considering both modes. For clarity, we do not show the TM and TE modes separately for the SOI₂ and bulk samples. With slight changes in the values of θ and τ_d the agreement with the experimental data is even better¹¹. We see that the reflectivities for the bulk and the SOI₂ samples are very similar, whereas the reflectivity of the SOI₁ sample is very different from the other two samples. This is because the

Symbol	Description	Value
ϵ_{Si}	dielectric constant	$13.6 + 0.048i^{16}$
β	TPA coefficient	$1.85 \times 10^{-9} \text{ cm/W}^{25}$
n_2	Kerr coefficient	$5 \times 10^{-15} \text{ cm}^2/\text{W}^{25}$
E_g	Band gap	1.12 eV^{26}
τ_d	carrier collision time	1.1 fs^7
θ	impact ionization coefficient	$21.2 \text{ cm}^2/\text{J}^{17}$

TABLE I. Material parameters used in the simulation as obtained from literature. The dielectric constant refers to unexcited silicon at a wavelength of 800 nm.

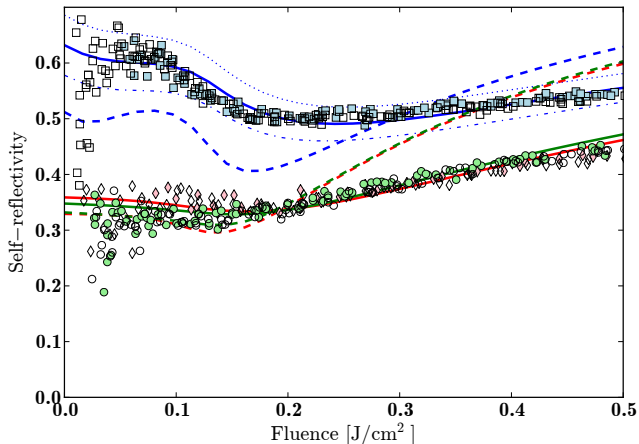


FIG. 4. 2D-FDTD calculations and experimental measurements of self-reflectivity for bulk silicon and silicon-on-insulator (SOI) samples. Open and closed symbols indicate results of two independent experimental runs for bulk silicon (circles), SOI₁ (squares) and SOI₂ (diamonds). The experimental errors are in all cases smaller than the symbols. The solid lines show the reflectivity calculated by 2D-FDTD simulations with the TM and TE modes combined for bulk (green), SOI₁ (blue) and SOI₂ (red). The dashed lines show the results obtained from a 1D-FDTD simulation. The blue dash-dotted and dotted lines show the reflectivity calculated for SOI₁ using either the TE or the TM mode, respectively.

device layer of the SOI₁ sample is thick enough to allow for constructive interference in the layer at 800 nm, impossible for the bulk sample and the 100nm device layer of the SOI₂ sample. As the incident fluence increases, the reflectivity drops to a minimum and then increases again. This behavior suggests a typical free-carrier (Drude) response. As the carrier density increases, the real part of the refractive index first drops until it reaches the critical density (where the plasma frequency equals the incident light frequency), after which the real part of the refractive index increases again. The dashed lines in Fig. 4 show the results of one-dimensional FDTD calculations using the same parameters as the two-dimensional calculations. The disagreement with the experimental data of the one-dimensional calculations directly shows that the wide range of incident angles must be taken into account when a high NA objective is used, as is the case in

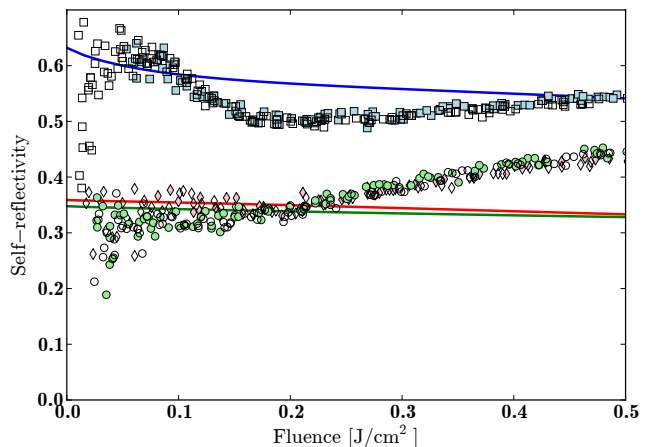


FIG. 5. FDTD calculations and experimental measurements of self-reflectivity on the SOI₁, SOI₂ and bulk samples. For the calculations, an impact ionization coefficient $\theta = 0 \text{ cm}^2/\text{J}$ is used. The lines and symbols have the same meaning as in Fig. 4.

nano-ablation experiments.

Parameter	Specified (Measured)	Adjusted
d_1 , SOI ₁	200 nm ($201.3 \pm 4.1 \text{ nm}$)	200 nm
d_2 , SOI ₁	1000 nm	970 nm
d_1 , SOI ₂	100 nm ($111.5 \pm 3.0 \text{ nm}$)	100 nm
d_2 , SOI ₂	300 nm	275 nm

TABLE II. Sample parameters. The device layer thicknesses d_1 are measure using atomic force microscopy. The specified values are also shown. For the buried oxide layer, only the specified values are given. We use the specified parameters for the device layer thicknesses and adjust the buried oxide layer to obtain the correct reflectivity in the low fluence limit.

To elucidate the important role of impact ionization in the carrier creation process, we show in Fig. 5 the calculation results with the impact ionization coefficient θ set to zero. The disagreement with the experimental data in Fig. 5 and the excellent agreement with the experimental data in Fig. 4 demonstrates directly that impact ionization plays a significant role in the development of the dense electron-hole plasma in silicon induced by a single femtosecond laser pulse. It should be pointed out that in earlier work⁷ the role of impact ionization was ignored, which resulted in an underestimation of the carrier density and a fitted (static) optical effective mass of $m^* = 0.18m_e$. However, as shown by Riffe's theoretical work, at a carrier temperature of 3000 K the optical effective mass of silicon already exceeds $0.24m_e$ ²¹. Considering that carrier temperature of above 10^4 K are reached in the experiments^{6,7}, the value $m^* = 0.18m_e$ reported in Ref.⁷ is far too low. To see whether these conditions also occur in our model, we inspect the carrier density and the carrier temperature as calculated in our model. In Fig. 6, we plot the results of those quantities. Specif-

ically, we plot the values obtained at the surface of the sample, directly after the pulse. In Fig. 6 (a) we find that the carrier density is clearly beyond 10^{22} cm^{-3} at the excitation level relevant for this work.

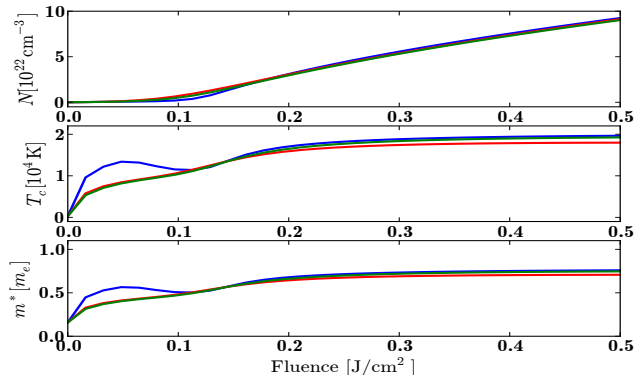


FIG. 6. Calculated a) carrier density, b) carrier temperature and c) optical effective mass on the surface of the sample after the end of the pulse. In each plot the green line shows the data for bulk silicon sample, the blue line for the SOI₁ sample and the red line for the SOI₂ sample.

In Fig. 6 (b), we see that the calculated carrier temperature is indeed larger than 10^4 K for all but the lowest fluences. Finally, in Fig. 6 (c), we plot the optical effective mass obtained from our model. It is also clearly beyond its unperturbed value ($0.15m_e$). This is caused by the high temperature reached in the laser-induced plasma.

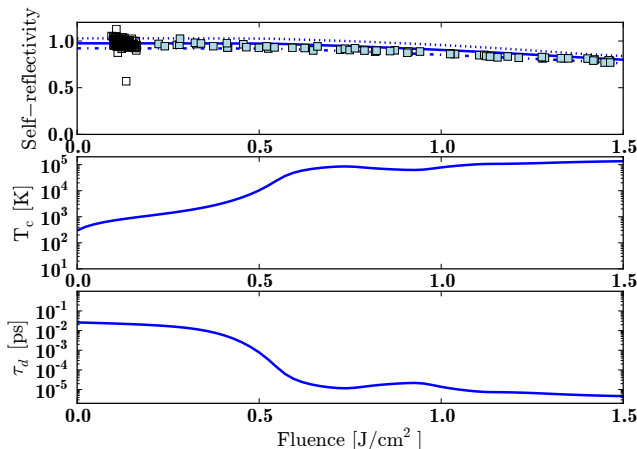


FIG. 7. (a) FDTD calculation and experimental measurements of self-reflectivity on a 400 nm gold film on glass. Open and closed squares are the experimental data from two independent runs. The solid line shows the calculated self-reflectivity taking both the TM and the TE mode into account. The dotted and dash-dotted lines show the self-reflectivity taking only the TM mode or only the TE mode into account, respectively. (b) Model calculated electron temperature on the surface of the sample. (c) The corresponding Drude damping time.

To test the versatility of our method, we also carried

out experiments and simulations on a 400 nm thick gold film grown on a glass substrate using vapor deposition. As mentioned in Sec. III B, the case for metals is simpler than that of semiconductors, as there is already such a high carrier concentration that only the heating of those carriers has an influence on the optical properties of the samples. In Fig. 7 (a) we can clearly see this simplicity in the experimental results: the self-reflectivity starts out high for low fluences and decreases slowly with increasing fluence. The lines in the plot are the results from our model, where no free parameters were used. All parameters, as listed in Table III, were taken from literature. We can see that the model excellently predicts the self-reflectivity from the unperturbed reflectivity without free parameters. The calculation also yields the electron temperature and the Drude damping time as shown in Fig. 7(b) and (c), respectively. We find also in the case of gold, temperatures beyond 10^4 K for all but the lowest fluences. Surprisingly, we find in Fig. 7(b) that the final carrier temperature T_c at the surface is not a monotonically rising function of incident fluence, but shows a slight decrease between fluence of 0.7 and 1.0 J/cm^2 . We attribute this reduction to the fact that at temperatures of $T > 10^4 \text{ K}$, the carrier damping time τ_d becomes shorter than the optical period. This means that above these temperatures, the imaginary part of the dielectric function and thus the absorption of the gold actually drop as a function of electron temperature.

Symbol	Value
ϵ_∞	6
A	$1.18 \times 10^7 \text{ s}^{-1} \text{ K}^{-222}$
B	$1.25 \times 10^{11} \text{ s}^{-1} \text{ K}^{-222}$
N	$5.9 \times 10^{22} \text{ cm}^{-3}$
$m^* m_e$	$1.1 m_e^{22}$

TABLE III. Physical parameters used in the simulation for gold. The coefficients A and B are as defined in the text around Eq. (21), N is the conduction electron density in gold, $m^* m_e$ is the optical effective mass and ϵ_∞ is an offset to the Drude dielectric constant that takes resonances at higher optical frequencies into account.

V. SUMMARY AND CONCLUSIONS

We presented a model describing the propagation and absorption of a strongly focused femtosecond laser pulse used for single-shot laser ablation in semiconductor and metal samples, based on a two-dimensional FDTD method. The model is compared with self-reflectivity measurements of strongly focused femtosecond laser pulses used for single-shot femtosecond laser ablation on two SOI samples, bulk silicon and gold. We obtain excellent agreement between simulation and experiments, using the unperturbed reflectivity to adjust material and sample specific constants; the self-reflectivity

at high fluences follows without the use of adjustable parameters. This confirms the accuracy and robustness of the model. The model clearly shows the dominant role of impact ionization for the carrier generation in silicon induced by a femtosecond laser pulse of 800 nm. Furthermore, the model demonstrates a marked increase of the optical effective mass due to the elevation of the carrier temperature during the pulse.

These results prove that FDTD simulations incorporating production and heating of free carriers and the free-carrier Drude response excellently describe the behavior of the self-reflectivity of strongly focused femtosecond laser beams under the ablation conditions. As the simulations accurately predict the self-reflectivity, it also gives a detailed understanding of the energy deposition of femtosecond laser pulses in metals and semiconductors. In conclusion, this extended FDTD method is an indispensable tool in the study of femtosecond laser nanostructuring of materials.

Appendix A: Extracting the complex amplitude from FDTD simulation

The FDTD method calculates real-value, time-varying electric and magnetic fields. However, some relevant physical quantities, such as the intensity Eq.(6), are more conveniently expressed in the amplitude of the oscillation. We extract the amplitudes of the fields from the simulation as follows. If we assume the amplitude is slowly varying with respect to the optical cycle, we can write the electric field on time t as

$$E(t) = E_0 \cos(\omega_0 t + \phi), \quad (\text{A1})$$

where ω_0 is the frequency of the light, and E_0 and ϕ are the amplitude and phase, respectively. If we integrate $E^2(t)$ over half an optical cycle $T/2$, we find

$$\begin{aligned} \int_0^{T/2} E^2(t) dt &= \int_0^{T/2} E_0^2 \cos^2(\omega_0 t + \phi) dt \\ &= \frac{1}{4} T E_0^2, \end{aligned} \quad (\text{A2})$$

and thus

$$E_0 = \sqrt{\frac{4 \int_0^{T/2} E^2(t) dt}{T}}. \quad (\text{A3})$$

In the FDTD simulation, the integration is approximated as a summation

$$\int_0^{T/2} E^2(t) dt \cong \sum_{n=n_1}^{n_1+m} E^2(n\Delta t) \cdot \Delta t, \quad (\text{A4})$$

where n_1 is the starting time step of the summation and m is the total time steps contained in half an optical cycle.

To extract the phase ϕ we consider the integral

$$\int_0^{T/2} E_0 \cos(\omega_0 t + \phi) e^{-i\omega_0 t} dt = \frac{E_0 \pi}{2\omega_0} (\cos \phi + i \sin \phi). \quad (\text{A5})$$

Thus, the phase of the electric field is the phase of above integral.

Appendix B: FDTD accuracy

The FDTD method has intrinsic second-order accuracy because it uses central difference for both the time and space derivative. A second source of error of a FDTD code is the small residual reflection at the PML boundary. In this appendix, we analyze the numerical error due to the FDTD algorithm. Based on this result, we deduce the right grid size and PML thickness for the simulations performed in this paper. To analyze the error, we calculate the reflectivity of a plane wave under normal incidence using one-dimensional FDTD method and compare the result to the exact Fresnel result²⁷

$$R = \left(\frac{n-1}{n+1} \right)^2, \quad (\text{B1})$$

which for silicon at 800 nm incident wavelength yields a reflectivity of 0.3287. The one-dimensional FDTD simulation space we use consists 50 nm of vacuum and 1 μm silicon, sandwiched between two PML layers. In order to extract the reflectivity, we carry out the simulations with and without the silicon layer. In the simulations we record the time-varying E and H field at the detector which is located one grid space above the silicon/vacuum interface. Thus the reflected time-varying Poynting vector is

$$S_{\text{ref}} = (E - E_{\text{free}}) \times (H - H_{\text{free}}), \quad (\text{B2})$$

where E_{free} and H_{free} are the fields from the simulation without the silicon layer. To obtain the reflectivity, we integrate the Poynting vectors S_{ref} over time

$$F = \int S_{\text{ref}} dt, \quad F_0 = \int S_{\text{free}} dt, \quad (\text{B3})$$

and write $R' = F/F_0$. The absolute error err in the FDTD simulation is then defined as

$$\text{err} = R' - R. \quad (\text{B4})$$

We run the simulation with a range of different grid spacings Δx and PML layer thicknesses n_{pml} measured in the number of cells in the PML layer. The pulse duration is set to 100 fs. The electric field of this pulse is used as a soft source²⁴ to excite the grid. Fig. 8 shows the resulting absolute error in reflectivity. From the figure we can see that for a coarser grid, the error is very large even for the thickest PML layer while for the finest grid, decreasing the PML thickness gives rise to larger error.

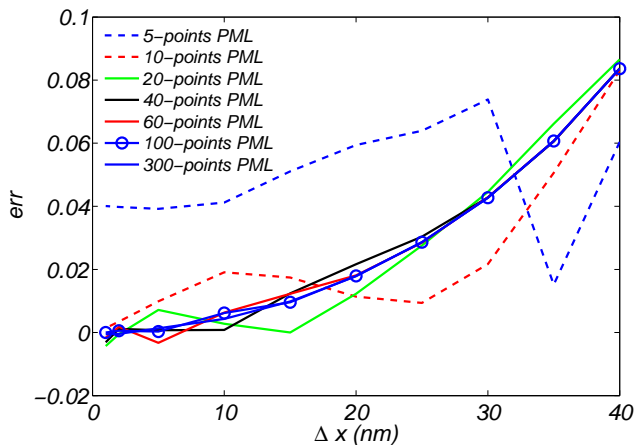


FIG. 8. The error of the FDTD method. Results with a range of PML thicknesses are presented.

This suggests that for a coarser grid the error from central difference approximation dominates while for a fine grid, the error from the PML layer dominates. To make the FDTD simulation very accurate, one needs to choose a fine grid and at the same time choose a thick PML layer. From the figure, we conclude that in order to keep the error in the absolute reflectivity smaller than 0.01, one needs a grid spacing ≤ 15 nm and a PML layer not less than 20 points.

Appendix C: Benchmark

Structure	R_{TM}	R'_{TM}	R_{TE}	R'_{TE}
Bulk Si	0.322	0.338	0.345	0.356
SOI	0.499	0.505	0.495	0.507
SOI*	0.220	0.237	0.236	0.252

TABLE IV. A comparison between the results of our 2D-FDTD code with the results from the commercial software FDTD Solutions. The results by FDTD Solutions are denoted by R'_{TM} and R'_{TE} . The * symbol represents the presence of a micron-sized scatterer embodied in the SOI wafer.

We developed the 2D-FDTD code based on the method described in the next Appendix. As a test for the validity of the 2D-FDTD code, we calculate the reflectivity of both unperturbed SOI with a 230 nm thick device layer and unperturbed bulk silicon with our FDTD code and compare the results with a commercial FDTD solver²⁸. The oxide layer of the SOI wafer is 1 μ m. We use a one-dimensional Gaussian profile of the electric field as a soft source to excite the simulation. The 1/e width of the Gaussian pulse is set to 100 fs. The grid size in the simulation is set as 13 nm. We extract the reflectivity from the field values calculated by the simulations. The results are summarized in Table IV. We further tested the code by calculating the reflectivity of a micron-sized

scatterer (dispersive and lossy) embodied in the device layer of the SOI wafer. As can be seen, the results obtained by the FDTD Solutions and our FDTD code are very close to each other. The small differences are most likely due to differences in PML layer thicknesses and/or the grid spacing.

Appendix D: Dispersive and lossy media

In two dimensions, the Maxwell's equations reduce to independent equations for the TM and TE modes²⁷. For the TM mode, these become²⁴

$$\frac{\partial \tilde{D}_z}{\partial t} = \frac{1}{\sqrt{\epsilon_0 \mu_0}} \left(\frac{\partial H_y}{\partial x} - \frac{\partial H_x}{\partial y} \right), \quad (D1)$$

$$\tilde{D}_z(\omega) = \epsilon_r^*(\omega) \tilde{E}_z(\omega), \quad (D2)$$

$$\frac{\partial H_x}{\partial t} = -\frac{1}{\sqrt{\epsilon_0 \mu_0}} \frac{\partial \tilde{E}_z}{\partial y}, \quad (D3)$$

$$\frac{\partial H_y}{\partial t} = \frac{1}{\sqrt{\epsilon_0 \mu_0}} \frac{\partial \tilde{E}_z}{\partial x}. \quad (D4)$$

Whereas for the TE mode they become

$$\frac{\partial \tilde{D}_x}{\partial t} = \frac{1}{\sqrt{\epsilon_0 \mu_0}} \frac{\partial H_z}{\partial y}, \quad (D5)$$

$$\frac{\partial \tilde{D}_y}{\partial t} = -\frac{1}{\sqrt{\epsilon_0 \mu_0}} \frac{\partial H_z}{\partial x}, \quad (D6)$$

$$\tilde{D}_x(\omega) = \epsilon_r^*(\omega) \tilde{E}_x(\omega), \quad (D7)$$

$$\tilde{D}_y(\omega) = \epsilon_r^*(\omega) \tilde{E}_y(\omega), \quad (D8)$$

$$\frac{\partial H_z}{\partial t} = -\frac{1}{\sqrt{\epsilon_0 \mu_0}} \left(\frac{\partial \tilde{E}_y}{\partial x} - \frac{\partial \tilde{E}_x}{\partial y} \right). \quad (D9)$$

In the above equations, we introduce scalar electric and displacement fields as

$$\tilde{\mathbf{E}} = \sqrt{\frac{\epsilon_0}{\mu_0}} \mathbf{E}, \quad (D10)$$

$$\tilde{\mathbf{D}} = \frac{1}{\sqrt{\epsilon_0 \mu_0}} \mathbf{D}, \quad (D11)$$

to make the electric and magnetic fields the same order of magnitude.

Note that Eqs. (D2), (D7) and (D8) are expressed in the frequency domain whereas the FDTD method works in the time domain. To bring the frequency domain equations into the time domain, we need to assume they are off a known analytical form. Here, we use a Drude model

$$\begin{aligned} \epsilon_{\text{ex}} &= \epsilon_{\text{Si}} + \chi_{\text{Drude}} \\ &= \epsilon_{\text{Si}} - \left(\frac{\omega_p}{\omega} \right)^2 \frac{1}{1 + i \frac{1}{\omega \tau}}. \end{aligned} \quad (D12)$$

Using partial fraction expansion and switching the imaginary unit from i to j ($j = -i$, as is conventional in

engineering), Eq. (D12) can be written as

$$\begin{aligned}\epsilon_{\text{ex}} &= \epsilon_{\text{Si}} + \frac{\omega_p^2 \tau}{j\omega} - \frac{\omega_p^2 \tau^2}{1 + j\omega\tau} \\ &= \epsilon_{\text{Si}} + \frac{\sigma_{\text{Drude}}}{j\omega\epsilon_0} + \frac{\chi}{1 + j\omega\tau}.\end{aligned}\quad (\text{D13})$$

Where we introduced the parameters

$$\sigma_{\text{Drude}} = \epsilon_0 \omega_p^2 \tau, \quad (\text{D14})$$

$$\chi = -\omega_p^2 \tau^2, \quad (\text{D15})$$

where σ_{Drude} is the conductivity of the plasma. The χ term causes additional dispersion. This is referred to as the Debye formulation²⁴ of the Drude model. Inserting this dielectric function, the electric displacement reads

$$\begin{aligned}D(\omega) &= \epsilon_{\text{ex}}(\omega)E(\omega) \\ &= \epsilon_{\text{Si}}E(\omega) + \frac{\sigma_{\text{Drude}}}{j\omega\epsilon_0}E(\omega) + \frac{\chi}{1 + j\omega\tau}E(\omega) \\ &= D'(\omega) + S(\omega),\end{aligned}\quad (\text{D16})$$

where the first two terms of the right-hand side of the equation are summarized as $D'(\omega)$ and the last term is written as $S(\omega)$.

As the FDTD operates in the time domain, Eq. (D16) must be transformed into the time domain. We first transform $D'(\omega)$ into the time domain. Recall that $\frac{1}{j\omega}$ in the frequency domain corresponds to integration in the time domain, so $D'(\omega)$ becomes

$$D'(t) = \epsilon_{\text{Si}}E(t) + \frac{\sigma_{\text{Drude}}}{\epsilon_0} \int_0^t E(t')dt'. \quad (\text{D17})$$

This integral is approximated as a summation over the time steps Δt

$$D'^n = \epsilon_{\text{Si}}E^n + \frac{\sigma_{\text{Drude}}\Delta t}{\epsilon_0} \sum_{i=0}^n E^i, \quad (\text{D18})$$

where n indicates the time step at $t = n\Delta t$. In the FDTD algorithm, we use this equation to determine the current E^n from the current D'^n and the previous values of E . We do this by first separating the E^n term from the rest of the summation

$$D'^n = \epsilon_{\text{Si}}E^n + \frac{\sigma_{\text{Drude}}\Delta t}{\epsilon_0}E^n + \frac{\sigma_{\text{Drude}}\Delta t}{\epsilon_0} \sum_{i=0}^{n-1} E^i, \quad (\text{D19})$$

and solving that equation for E^n

$$E^n = \frac{D'^n - \frac{\sigma_{\text{Drude}}\Delta t}{\epsilon_0} \sum_{i=0}^{n-1} E^i}{\epsilon_{\text{Si}} + \frac{\sigma_{\text{Drude}}\Delta t}{\epsilon_0}}. \quad (\text{D20})$$

We now treat the $S(\omega)$ term in Eq. (D16) in a similar manner. We convert the term

$$S(\omega) = \frac{\chi}{1 + j\omega\tau}E(\omega), \quad (\text{D21})$$

to the time domain to find

$$S(t) = \frac{\chi}{\tau} \int_0^t e^{-\frac{t-t'}{\tau}} E(t')dt'. \quad (\text{D22})$$

We approximate the integral as a summation

$$\begin{aligned}S^n &= \chi \frac{\Delta t}{\tau} \sum_{i=0}^n e^{-\frac{\Delta t(n-i)}{\tau}} E^i \\ &= \chi \frac{\Delta t}{\tau} \left[E^n + \sum_{i=0}^{n-1} e^{-\frac{\Delta t(n-i)}{\tau}} E^i \right].\end{aligned}\quad (\text{D23})$$

We can add Eq. (D23) to Eq. (D19) to find the electric displacement for all the three terms

$$\begin{aligned}D^n &= \epsilon_{\text{Si}}E^n + \frac{\sigma_{\text{Drude}}\Delta t}{\epsilon_0}E^n + \frac{\sigma_{\text{Drude}}\Delta t}{\epsilon_0} \sum_{i=0}^{n-1} E^i \\ &\quad + \chi \frac{\Delta t}{\tau} \left[E^n + \sum_{i=0}^{n-1} e^{-\frac{\Delta t(n-i)}{\tau}} E^i \right],\end{aligned}\quad (\text{D24})$$

which when we solve for E^n yields

$$E^n = \frac{D^n - \frac{\sigma_{\text{Drude}}\Delta t}{\epsilon_0} \sum_{i=0}^{n-1} E^i - \chi \frac{\Delta t}{\tau} \sum_{i=0}^{n-1} e^{-\frac{\Delta t(n-i)}{\tau}} E^i}{\epsilon_{\text{Si}} + \frac{\sigma_{\text{Drude}}\Delta t}{\epsilon_0} + \chi \frac{\Delta t}{\tau}}. \quad (\text{D25})$$

As in the case of pure damping, we calculate E^n (the current value of E) from the current value of D and the summation of all previous values of E .

We can easily describe two-photon absorption (TPA) and the optical Kerr effect into Eq. (D25) by introducing an extra conductivity term due to the TPA and an extra change in the real part of the dielectric constant due to the optical Kerr effect. Together with the one-photon absorption (OPA), Eq. (D25) can finally be written as

$$E^n = \frac{D^n - \frac{\sigma\Delta t}{\epsilon_0} \sum_{i=0}^{n-1} E^i - \chi \frac{\Delta t}{\tau} \sum_{i=0}^{n-1} e^{-\frac{\Delta t(n-i)}{\tau}} E^i}{\text{Re}[\epsilon_{\text{Si}}] + \Delta\epsilon + \frac{\sigma\Delta t}{\epsilon_0} + \chi \frac{\Delta t}{\tau}}. \quad (\text{D26})$$

Where $\sigma = \sigma_{\text{OPA}} + \sigma_{\text{TPA}} + \sigma_{\text{Drude}}$ and $\Delta\epsilon$ is the change in the real part of the dielectric constant due to the optical Kerr effect. The term σ_{OPA} can be linked to the imaginary part of the dielectric constant of un-excited silicon. The terms $\Delta\epsilon$ and σ_{TPA} are linked to the real and imaginary part of $\chi^{(3)}$, respectively.

Appendix E: Spatial filtering

In the simulation, interaction between the light and the localized laser-induced plasma gives rise to field components with high spatial-frequencies. When we decompose the wave vector into the transverse and the longitudinal component they are related by

$$k_x = \sqrt{k^2 - k_y^2}, \quad (\text{E1})$$

where k is the wavenumber in air and k_y is the transverse wavenumber. We observe from the above equation that for $k_y^2 > k^2$ the longitudinal wavenumber k_x is purely imaginary, therefore the wave associated with it is evanescent and will not propagate into the far-field. Prior to calculating the reflectivity, these components should therefore be filtered out. The transverse wavenumber can be conveniently written as $k_y = k \sin \theta$, where θ is the angle of reflection. As the numerical aperture of the objective used in our experiments is $\text{NA} = \sin \theta = 0.8$. This means that scattered waves associated with a transverse wavenumber $k_y > 0.8k$ will not be collected by the objective. This means that what is measured in Figs. 4 and 7 is in fact the scattered field associated with a transverse wavenumber $k_y < 0.8k$. So in the FDTD simulation, spatial-frequency components with $k_y > 0.8k$ should be filtered out. This is accomplished by the spectral decom-

position fields²⁹

$$\widehat{A}(k_y) = \frac{1}{\sqrt{2\pi}} \int_{-\infty}^{\infty} A(y) e^{-ik_y y} dy, \quad (\text{E2})$$

and transforming this composition back using a truncated inverse Fourier transform

$$A'(y) = \frac{1}{\sqrt{2\pi}} \int_{-0.8k}^{0.8k} \widehat{A}(k_y) e^{ik_y y} dk_y. \quad (\text{E3})$$

ACKNOWLEDGMENTS

We thank Cees de Kok and Paul Jurrius for discussions and technical assistance. We thank Sandy Pratama for proof-reading the manuscript. HZ acknowledges the financial support from China Scholarship Council. DMK acknowledges support from NSF grant DMR 1206979.

-
- * Electronic mail: zhterran@qq.com
 † Corresponding author: D.vanOosten@uu.nl
- ¹ E. G. Gamaly, S. Juodkazis, K. Nishimura, H. Misawa, B. Luther-Davies, L. Hallo, Ph. Nicolai, and V. T. Tikhonchuk, *Phys. Rev. B* **73**, 214101 (2006)
 - ² Y. Liao, Y. Shen, L. Qiao, D. Chen, Y. Cheng, K. Sugioka, and K. Midorikawa, *Opt. Lett.* **38**, 187 (2013).
 - ³ H. Zhang, D. van. Oosten, D. M. Krol, and J. I. Dijkhuis, *Appl. Phys. Lett.* **99**, 231108 (2011).
 - ⁴ M. Li, K. Mori, M. Ishizuka, X. Liu, Y. Sugimoto, N. Ikeda, and K. Asakawa, *Appl. Phys. Lett.* **83**, 216 (2003)
 - ⁵ B. Rethfeld, K. Sokolowski-Tinten, D. Von Der Linde, and S. I. Anisimov, *Appl. Phys. A* **79**, 767 (2004).
 - ⁶ D. Hulin, M. Combescot, J. Bok, A. Migus, J. Y. Vinet and A. Antonetti, *Phys. Rev. Lett.* **52**, 1998 (1984).
 - ⁷ K. Sokolowski-Tinten and D. von der Linde, *Phys. Rev. B* **61**, 2643 (2000).
 - ⁸ K. Sokolowski-Tinten, J. Bialkowski, and D. von der Linde, *Phys. Rev. B* **51**, 14186 (1995).
 - ⁹ R. W. Boyd, *Nonlinear Optics* (3rd edition), Academic Press, Orlando, 2008.
 - ¹⁰ Th. Brabec and F. Krausz, *Phys. Rev. Lett.* **78**, 3282 (1997).
 - ¹¹ H. Zhang, D. M. Krol, J. I. Dijkhuis, and D. van Oosten, *Opt. Lett.* **38**, 5032 (2013)
 - ¹² L. Hallo, A. Bourgeade, V. T. Tikhonchuk, C. Mezel, and J. Breil, *Phys. Rev. B*, **76**, 024101 (2007).
 - ¹³ C. Mézel, L. Hallo, A. Bourgeade, D. Hébert, V. T. Tikhonchuk, B. Chimier, B. Nkonga, G. Schurtz, and G. Travaill, *Phys. Plasmas*, **15**, 093504 (2008).
 - ¹⁴ I. B. Bogatyrev, D. Grojo, P. Delaporte, S. Leyder, M. Sentis, W. Marine, and T. E. Itina *J. Appl. Phys.* **110**, 103106 (2011)
 - ¹⁵ H. Schmitz and V. Mezentsev, *J. Opt. Soc. Am. B*, **29** 1208 (2012)
 - ¹⁶ T. Y. Choi and C. P. Grigoropoulos, *J. Appl. Phys.* **92**, 4918 (2002); T. Y. Choi and C. P. Grigoropoulos, *J. Heat Transfer*, 126, 723 (2004)
 - ¹⁷ P. P. Pronko, P. A. VanRompay, C. Horvath, F. Loesel, T. Juhasz, X. Liu, and G. Mourou, *Phys. Rev. B* **58**, 2387 (1998).
 - ¹⁸ N. Medvedev and B. Rethfeld, *J. Appl. Phys.* **108**, 103112 (2010)
 - ¹⁹ B. C. Stuart, M. D. Feit, S. Herman, A. M. Rubenchik, B. W. Shore, and M. D. Perry, *Phys. Rev. B* **53**, 1749 (1996).
 - ²⁰ N. W. Ashcroft and N. D. Mermin, *Solid State Physics*. Philadelphia: Saunders College, 1976.
 - ²¹ D. M. Riffe, *J. Opt. Soc. Am. B* **19**, 1092 (2002).
 - ²² K. Vestenft and P. Balling, *Appl. Phys. A* **84**, 207 (2006).
 - ²³ Z. Lin, L. V. Zhigilei, and V. Celli, *Phys. Rev. B* **77**, 075133 (2008). Updated calculations at <http://www.faculty.virginia.edu/CompMat/electron-phonon-coupling/>
 - ²⁴ D. M. Sullivan, *Electromagnetic simulation using the FDTD method*, IEEE press, 2000.
 - ²⁵ A. D. Bristow, N. Rotenberg and H. M. Van Driel, *Appl. Phys. Lett.* **90**, 191104 (2007).
 - ²⁶ H. M. van Driel, *Phys. Rev. B* **35**, 8166 (1987).
 - ²⁷ M. Born and E. Wolf, *Principles of Optics*, Cambridge University Press, Cambridge, 1999.
 - ²⁸ Lumerical Solutions, Inc. <http://www.lumerical.com/tcad-products/fdtd/>
 - ²⁹ L. Novotny and B. Hecht, *Nano Optics* (Cambridge University Press, Cambridge, 2006).